A New Parameterization of Photolysis Rates for Oxygenated Volatile Organic Compounds (OVOCs)

Yuwen Peng [1], Bin Yuan [1,*], Sihang Wang [1], Xin Song [1], Zhe Peng [1],

Wenjie Wang [2], Suxia Yang [1], Jipeng Qi [1], Xianjun He[1], Yibo Huangfu [1],

Xiao-Bing Li [1], Min Shao [1,*]

[1] College of Environment and Climate, Institute for Environmental and Climate Research, Guangdong-Hongkong- Macau Joint Laboratory of Collaborative Innovation for Environmental Quality, Jinan University, 51143, China

[2] Multiphase Chemistry Department, Max Planck Institute for Chemistry, Mainz 55128, Germany

Correspondence to: Bin Yuan (byuan@jnu.edu.cn) and Min Shao (mshao@pku.edu.cn)

Abstract:

Oxygenated volatile organic compounds (OVOCs) play a crucial role in atmospheric chemistry, significantly influencing radical production and VOC degradation through photolysis. However, current research on OVOC photolysis is limited by insufficient species coverage in the mechanisms and incomplete understanding from a species-specific perspective. In this study, the photolysis frequencies of 109 OVOCs were compiled into a comprehensive photolysis dataset. Based on their molecular structures, a parameterization for the photolysis frequencies of carbon- and nitrogen-containing OVOCs was developed. By establishing a relationship between species structure and photolysis frequency, this approach avoids the limitation of insufficient quantum yield data, enabling the estimation of photolysis rate constants for compounds lacking experimental measurements. Photolysis frequencies for the dataset species were successfully reproduced with 21 reference values and 10 adjustment coefficients. Using an automated program based on this method, photolysis rate constants for 3039 OVOCs were predicted, and the MCM v3.3.1 chemical mechanism was updated and expanded to include photolysis for 714 additional species. The introduction of the new photolysis mechanism has altered both the concentrations of photodegradable OVOCs and the relative proportions of their removal pathways. Non-HCHO OVOCs, particularly multifunctional species with carbonyl groups, contribute significantly to ROx radical production. At three different sites, non-HCHO OVOCs photolysis accounts for 25%-45% of ROx production, surpassing HCHO photolysis. The importance of oxidation products from aromatics and alkenes is highlighted, offering new insights into OVOCs photolysis from a species-specific perspective.

Keywords:

OVOCs photolysis, Parameterization, Box model, ROx radicals

1.Introduction

Oxygenated volatile organic compounds (OVOCs) are a subset of VOCs and encompass a range of compounds, including aldehydes, ketones, alcohols, acids, ethers, esters, and highly reactive species such as enals and enones. They significantly affect atmospheric chemistry and contribute to the formation of secondary pollution (Mellouki et al., 2015; Huang et al., 2020). OVOCs originated not only from the oxidation of hydrocarbons but also from primary emissions (Mcdonald et al., 2018). OVOCs are characterized by their diverse species, high reactivity, complex sources, and measurement difficulty. With the advancement of modern mass spectrometry technologies, the importance of OVOCs is gradually revealing, contributing 16%–51% to the total concentrations of VOCs in different environments (Liu et al., 2020; Li et al., 2020; Hui et al., 2018; Jing et al., 2020; Song et al., 2023). OVOCs are removed from the atmosphere through reactions with oxidants, wet or dry deposition, and photolysis (Mellouki et al., 2015). The photolysis rate influences the relative importance of removal pathways for photodegradable OVOCs. For some species, photolysis serves as the dominant sink and governs their atmospheric fates (Yuan et al., 2016; Eger et al., 2020).

Through photolysis, OVOCs can produce atmospheric radicals such as RO_2 and HO_2, which enhance atmospheric oxidation capacity and contribute to ozone formation (Tan et al., 2019a; Tan et al., 2019b; Kanaya et al., 2007; Griffith et al., 2016). The photolysis of OVOCs plays a significant role in the production of ROx radicals (ROx $= RO_2 + HO_2 + OH$) (See Figure 1 and Table S1) and can account for over 80% of the production of ROx (p(ROx)) during the later stages of winter ozone pollution (Edwards et al., 2014). OVOCs from different sources play varying roles in their contributions to atmospheric oxidation capacity. Primarily emitted OVOCs act as primary radical producers, capable of directly generating 1 to 2 radicals through photolysis, resulting in a net production of radicals. This net production provides a substantial supply of radicals for the initial oxidation processes in atmospheric chemistry (Mellouki et al., 2015). Meanwhile, OVOCs formed through secondary processes serve as

72   "photochemical amplifiers" accelerating the formation of secondary pollutants. OVOCs

73   produced from oxidation may undergo photolysis to produce additional radicals, further

74   contributing to formation of more OVOCs (Qu et al., 2021). This creates a positive

75   feedback loop that has been recognized as a key factor in high winter ozone

76   concentrations in multiple regions (Edwards et al., 2014; Li et al., 2021). Furthermore,

77   as primary radical producers, OVOCs photolysis increases the production of ROx,

78   while as photochemical amplifiers, they increase radical chain length. Thus, the

79   photolysis of OVOCs effectively enhances atmospheric oxidation capacity.

80   However, several challenges remain that hinder our ability to better constrain the

81   environmental effects of OVOCs photolysis. Firstly, current chemical mechanisms fail

82   to fully account for recently reported photodegradable species, such as some

83   multifunctional compounds (Newland et al., 2019; Tomas et al., 2021; Müller et al.,

84   2014; Wang et al., 2023). Traditional mechanisms mainly focus on mono- or bi-

85   functional, low-carbon species (See Section S1 and Figure S9 of *Supplementary*

86   *Information*). Secondly, significant discrepancies exist in the reported photolysis

87   frequencies of certain species (e.g., nitrophenol or benzaldehyde (Peng et al., 2023;

88   Mellouki et al., 2015). These differences largely arise from varying estimates of

89   quantum yield, which can lead to differences in photolysis rate constants by nearly an

90   order of magnitude. Furthermore, many species remain unmeasured or lack sufficient

91   reporting. Although the development of modern measurement techniques has greatly

92   expanded the range of measurable species (Ye et al., 2021; Yuan et al., 2017), it is still

93   prohibitively expensive in terms of time and cost to measure photodegradable species

94   individually. Currently, the MPI-Mainz UV/VIS database includes absorption cross-

95   section data for 310 organic compounds, but quantum yield information is only

96   available for formaldehyde and acetaldehyde (Keller-Rudek et al., 2013). Similarly, the

97   IUPAC database provides absorption cross-sections and photolysis product data for 39

98   compounds, yet more than half of these species lack recommended quantum yield

99   values or assume a quantum yield of 1 across all wavelengths (IUPAC, 2012). The

100   scarcity and uncertainty of quantum yield data remain significant limitations in deriving

101 accurate photolysis rate constants for OVOCs. Finally, due to the incomplete
102 description of mechanisms, current evaluations for the contribution of OVOCs
103 photolysis to atmospheric oxidation capacity primarily focus on simple species such as
104 formaldehyde (Tan et al., 2019a; Young et al., 2012), or treat OVOCs as a whole (Liu
105 et al., 2012; Yang et al., 2018).

106 Several parameterization approaches for OVOCs photolysis rate constants have
107 been developed, including Master Chemical Mechanism (MCM) (Jenkin et al., 1997;
108 Jenkin et al., 2003), the Generator for Explicit Chemistry and Kinetics of Organics in
109 the Atmosphere (GECKO-A) (Aumont et al., 2005), and the SAPRC mechanism
110 generation system (MechGen) (Carter et al., 2025). MCM v3.3.1 applies a core set of
111 20 reactions parameterized as functions of the solar zenith angle, with surrogate
112 parameters for species with limited data, but sometimes assigns identical rates to
113 structurally distinct compounds. GECKO-A focuses on three primary chromophores
114 (carbonyls, hydroperoxides, nitrates) and employs detailed cross-section datasets for 54
115 species, yet lacks differentiation among conjugated systems or less common
116 photodegradable functional groups. MechGen, developed specifically for the SAPRC
117 mechanism, assigns overall quantum yields to representative species based on grouped
118 reactivity. However, it assumes that quantum yields are wavelength-independent and
119 provides only lumped quantum yields rather than explicit photolysis rate constants.
120 Consequently, there is no comprehensive or easily accessible source for photolysis rate
121 constants of a specific OVOC species, as the existing data are dispersed across various
122 studies. These limitations highlight the need for a structure-specific approach that
123 directly outputs photolysis rate constants and captures a wide range of functional group
124 combinations.

125 In this study, we have integrated the most recently reported photolysis frequency
126 data to obtain a dataset of OVOCs photolysis. From this dataset, we establish a
127 relationship between the chemical structures of OVOCs and their photolysis rate
128 constants, avoiding the need for inaccessible quantum yield data across many species.
129 Based on this dataset, a new parameterization method was proposed to predict

130 photolysis frequencies based on molecular structures. Subsequently, these predicted
131 photolysis frequencies were incorporated into chemical mechanisms and were
132 evaluated using an observation-based box model to quantitatively assess the
133 atmospheric impacts.

2 Method

2.1 Observation

136   Field measurements were conducted at three sites, representing both urban and
137 regional environments in southern and northern China. The urban site in southern China
138 was located at the Guangzhou Institute of Geochemistry (GIG), Chinese Academy of
139 Sciences (23.1°N, 113.2°E) in the urban area of Guangzhou. Instruments were deployed
140 approximately 25 meters above ground level, and measurements were taken during the
141 fall of 2018 (September to November). The site was surrounded by residential areas
142 and roadways (Wu et al., 2020; Wang et al., 2020; Yang et al., 2022). The urban site in
143 northern China was in downtown Beijing, where a three-month field campaign was
144 conducted from May to August of 2021. The site was located at the Institute of
145 Atmospheric Physics (IAP), Chinese Academy of Sciences (23.15°N, 113.36°E), which
146 is a large meteorological and environmental monitoring tower in the bustling city center
147 (Li et al., 2025; Huangfu et al., 2024). Data collected from July 7 to July 31 at an
148 approximate height of 5 m above the ground was used in this study. The regional site
149 was the Guangdong Atmospheric Supersite (22.7°N, 112.9°E) situated in Heshan (HS),
150 approximately 80 km southwest of Guangzhou and frequently influenced by
151 anthropogenic emissions from the Guangzhou–Foshan megacity. Observations were
152 conducted during the fall of 2019 (October-November), characterizing it as a
153 representative regional receptor site in the Pearl River Delta (PRD) (Cai et al., 2024;
154 Yang et al., 2022).

155   OVOCs were measured at all three sites using a high-resolution proton-transfer-
156 reaction quadrupole interface time-of-flight mass spectrometer (PTR-QiToF-MS,
157 Ionicon Analytik, Austria) (Wu et al., 2020; He et al., 2022). At the Guangzhou urban
158 site and PRD regional site, non-methane hydrocarbons (NMHCs) were measured

159 hourly using a gas chromatograph equipped with a flame ionization detector and a mass

160 spectrometer (GC-MS-FID, Wuhan Tianhong Co., Ltd, China) (Wang et al., 2022).

161 NMHCs data from the Beijing urban site was unavailable so we estimated those

162 unmeasured species according to proton-transfer-reaction time-of-flight mass

163 spectrometer (PTR-ToF-MS) data, data from nearby stations, and OH reaction rate

164 constants (k_{OH}) of individual species with OH radicals. Detailed estimation methods are

165 provided in the Supporting Information of Li et al. (2025).

166 Details regarding the measurement of meteorological parameters, photolysis

167 rates, and trace gases at the three sites, including instruments used and specific

168 measurement methods, are provided in Section S2 of *Supplementary Information*.

169 Further details on the instruments used at each site are provided in Wang et al. (2022)

170 for the Guangzhou urban site, Yang et al. (2024) for the Beijing urban site, and Yang et

171 al. (2022) for the PRD regional site. Temporal variations of typical photodegradable

172 species at each site, along with reference parameters including Ox, NOx, O₃,

173 temperature, relative humidity, and j_{NO_2}, are presented in Figure S1.

174 **2.2 Box Model Description**

175 A zero-dimensional box model, built on the Framework for 0-D Atmospheric

176 Modeling (F0AM) v4.3 (Wolfe et al., 2016), was applied in this study to compare

177 mechanisms and evaluate their atmospheric impacts. The chemical mechanisms

178 included the MCM v3.3.1 (Jenkin et al., 2015; Bloss et al., 2005; Jenkin et al., 2003)

179 and the photolysis mechanism proposed in this study. MCM has been widely used for

180 modeling atmospheric radicals and secondary products (Aumont et al., 2005; Edwards

181 et al., 2014; Chen et al., 2022). The model was constrained using 5-minute averaged

182 relative humidity, ambient temperature, pressure, photolysis frequencies, and

183 concentrations of directly measured trace gases and VOCs (listed in Table S2).

184 Simulations were performed until steady-state conditions with a 3-day spin-up period

185 to allow for the buildup of unmeasured intermediate species (Yang et al., 2022). To

186 prevent the unrealistic accumulation of long-lived species, an empirically derived first-

187 order physical dilution coefficient k_{dil} was applied, with values of 1.2×10^{-5} s^{-1} for both

删除了: Master Chemical Mechanism (

删除了:)

190   urban sites (equivalent to a 24-hour lifetime) and 3.5×10^{-5} s^{-1} for the PRD regional site

191   (equivalent to an 8-hour lifetime) (Yang et al., 2022). In addition to the MCM v3.3.1

192   mechanism, photolysis reaction of ClNO$_2$ has been included, frequency of which is

193   derived by reducing the j_{NO_2} by a factor of 30 (Riedel et al., 2014).

194   In this study, we designed two model scenarios to explore atmospheric effects of

195   the newly proposed photolysis mechanism and to identify key species that significantly

196   contribute to the production of total radicals. Scenario 1 was designed to investigate the

197   impact of the new photolysis mechanism under traditional simulation settings. Among

198   all the OVOC species, only formaldehyde (HCHO) was constrained to its measured

199   concentrations. This setup allowed us to assess the impacts of the photolysis mechanism

200   on the atmospheric chemical simulations with the common practice, which facilitated

201   comparing our findings with other studies. However, a key limitation of Scenario 1 is

202   that it may not accurately simulate many organic intermediates. The inadequate

203   representation of these intermediates hindered a more detailed analysis of the key

204   species involved in atmospheric chemistry. To address this issue, Scenario 2 was

205   constrained by 20 additional non-HCHO OVOCs (listed in Table S4) based on PTR-

206   ToF-MS measurements and applied a dynamic allocation method to semi-quantitatively

207   estimate concentrations from PTR-ToF-MS, thereby constraining over 1300 OVOC

208   intermediates. A detailed description of the dynamic allocation method can be found in

209   Section S3 and Figure S10 of *Supplementary Information*. By incorporating a broader

210   range of OVOC constraints, Scenario 2 allowed for a more accurate representation of

211   atmospheric reactions and provided deeper insights into the role of OVOCs photolysis

212   in driving radical production. Aside from the differences in the constraints on OVOC

213   concentrations, both scenarios follow the same setup as described in the previous

214   section.

215   **2.3 Photolysis dataset for parameterization**

216   The photolysis frequencies can be calculated by numerical summation over

217   wavelength using Equation (1) (Calvert et al., 2002).

218   $$J = \int \delta_i \times \phi_i \times F_i \, d\lambda_i \qquad (1)$$

删除了:

220   δ_i, ϕ_i, and F_i stand for the absorption cross section, quantum yield, and spectral

221   actinic flux of the species i, respectively. The absorption cross-section and quantum

222   yield are typically obtained through laboratory measurements, while the actinic flux is

223   usually acquired through field measurements or models.

224   A dataset for OVOCs photolysis rate constants has been constructed for the

225   subsequent development of parameterization. The data within the dataset are collected

226   from databases like MPI-Mainz UV/VIS (Keller-Rudek et al., 2013) and IUPAC

227   (Mellouki et al., 2021), as well as from textbooks (Calvert et al., 2011) and other

228   relevant literature (See the *"Species Dataset"* sheet in the supplementary file for details).

229   The tropospheric ultraviolet and visible (TUV) radiation model (version 5.3)

230   (Madronich and Flocke, 1999; Lantz et al., 1996) was used to provide a spectral actinic

231   flux under a clear-sky condition. Before inclusion into the dataset, all data were

232   converted to the ratio of photolysis frequencies of OVOCs species under overhead sun

233   condition ($j_{OVOC,overhead}$) to those for the reference species ($j_{NO_2,overhead}$), which is

234   referred as the relative photolysis frequencies j_{rel} ($= j_{OVOC,overhead}/j_{NO_2,overhead}$).

235   The relative photolysis frequencies can be conveniently applied to different

236   environments by conversion with measured j_{NO_2}. The data inclusion process is depicted

237   in Section S4 and Figure S11 of *Supplementary Information*.

238   The photolysis dataset is divided into a reference group and a comparison group.

239   In the current photolysis dataset, the reference group encompasses a total of 195

240   photolysis rate constants data entries for 109 OVOCs species, including 5 pairs of

241   isomers. The comparison group includes 50 data entries covering 38 species from 8

242   reports. The reference group primarily consists of data from smog chamber

243   measurements and peer-reviewed recommended data, which will be used for the

244   construction of parameterization schemes. The data in the comparison group mainly

245   consists of the results measured at a single wavelength, results obtained by measuring

246   absorption cross-sections but estimating quantum yields, and estimates for entire

247   categories of substances, such as the single value provided by Treves and Rudich (2003)

248   for hydroxy nitrates containing 3 to 6 carbon atoms. Additionally, results from quantum

249 chemical calculations are also included in the comparison group. Since it mainly

250 includes data with larger uncertainties than the reference group, the comparison group

251 is only used for comparison and not for the construction of the parameterization.

252 For all OVOCs species in the dataset, the simplified molecular input line entry

253 system (SMILES) format is used to describe their molecular structures. SMILES is a

254 specification that uses ASCII strings to explicitly describe molecular structures. It is not

255 only capable of covering all chemical formulas, but also highly readable, easy to

256 understand, and has been adopted by many leading international chemical databases

257 (Weininger, 1988; Wang et al., 2018).

3 Results and discussion

3.1 Development of a structural-based parameterization method

260 An analysis of the relationship between the relative photolysis rate constant (j_{rel})

261 and species characteristics revealed no significant correlation between j_{rel} and the

262 number of oxygen atoms in the molecules. However, some aromatics, nitrates,

263 aldehydes, and hydroxy carbonyls show a slight increase in j_{rel} with rising carbon

264 oxidation states ($\overline{OS_c}$), calculated following the method of Kroll et al. (2011), while

265 other species display no significant trends. Interestingly, j_{rel} tend to increase with the

266 number of functional groups in the molecules, except for N-nitrosamines and alkyl

267 nitrites (Figure S2). Although no clear correlation was observed between j_{rel} and the

268 number of carbon atoms, compounds with similar functional groups tend to cluster

269 within a specific range of j_{rel} (Figure 2). When j_{rel} of the species in the same

270 compound class are averaged, distinct differences emerge between functional group

271 types, suggesting that the parameterization should focus on the types and quantities of

272 functional groups present in the species.

273 The photolysis data for OVOCs collected from multiple literature sources were

274 classified based on their functional groups. Compounds within the same family,

275 particularly those with similar functional groups, generally exhibit analogous

276 absorption cross-sections in the UV-visible spectrum (see Figure S3). This property

277 serves as an essential theoretical basis for structure-based estimation. During oxidation

processes, when new functional groups are added to existing molecular structures, conjugation may occur between different chromophores. Such interaction cannot be simply treated as the additive effects of two individual chromophores, making it necessary to discuss different conjugated systems categorically.

A comparison of data from different literature sources revealed consistent photolysis rate constants for most species, with notable differences observed for certain compounds, such as benzaldehyde, pyruvic acid, peracetic acid, and 2-butenedial (Figure S4). Based on the 195 entries in the OVOCs photolysis dataset, the reported values for the same compound from different literature sources were first averaged, obtaining the averaged data for 109 OVOCs ("*Averaged Dataset*" sheet in the supplementary file). The averaged j_{rel} for 109 compounds were then classified into 23 categories according to their functional group types. These j_{rel} form a dataset for the development of a more accurate parameterization.

Based on the summarized photolysis frequencies, the reference values for 21 classes of compounds were calculated to provide guidance for predicting the photolysis frequencies of the compounds in the same classes containing more carbon atoms. Taking the example of n-aldehydes, one of the most extensively studied groups, their absorption band appears in the UVB region (around 280 nm) due to a weak $n \rightarrow \pi^*$ electronic transition, overlapping partially with the tropospheric radiation spectrum (>290 nm) (Calvert et al., 2011). The absorption cross-sections of n-aldehydes containing 1 to 7 carbon atoms are shown in Figure S11. For formaldehyde (HCHO), the carbonyl carbon is attached with two hydrogen atoms, and the stretching vibration of the C=O double bond in the π^* excited state is particularly prominent in the absorption band, resulting in significant fluctuations in its absorption cross-section. As the carbon chain length increases, the stretching vibration of the C=O bond in the π^* excited state becomes less pronounced, and the absorption bands nearly overlap (Calvert et al., 2011). Although the absorption of n-heptanal (n-C_6H_{13}CHO) is slightly higher than that of n-pentanal, it is reasonable to consider that, for n-aldehydes, the absorption cross-sections and photolysis rate constants become similar once the carbon

313 number reaches 3 or higher. This assumption is consistent with a previous study (Tadić

314 et al., 2001). Therefore, in calculating the reference photolysis rate constants for the

315 aldehyde carbonyl group (-CHO), the average photolysis rate constants of aldehydes

316 with 3 to 7 carbons are used as the reference value $(0.18\% \pm 0.053\% \, jNO_2)$ for

317 aldehydes with 8 or more carbons. In addition to n-aldehydes, photolysis reference

318 values were calculated for other 20 classes of species, including substituted aldehydes

319 (e.g., nitrobenzaldehydes, aromatic aldehydes, unsaturated aldehydes, and dialdehydes),

320 nitrogen-containing compounds (e.g., N-nitrosamines, nitrophenols, nitroaromatics,

321 alkyl nitrites, carbonyl nitrates, and peroxy nitrates), ketones (e.g., diketones, cyclic

322 ketones, and unsaturated ketones), as well as other species such as dienedials, keto acids,

323 hydroperoxides, and peroxy acids (see Figure 3). The reference values for

324 corresponding species with 1 to 20 carbons are tabulated for clarity (See the *"Reference*

325 *Value Table"* sheet in the supplementary file). By establishing a relationship between

326 the photolysis rate constants and carbon number, the reference photolysis rate constants

327 for higher-carbon compounds are estimated. The calculation methods for these

328 functional groups are similar to those of aldehydes, with details provided in Section S5

329 and Figure S12-S30 of *Supplementary Information*. The parameterization is currently

330 applicable only to compounds composed of carbon (C), hydrogen (H), oxygen (O), and

331 nitrogen (N). Functional groups involving sulfur, halogens, or other elements are not

332 involved in this study, due to limited availability of data for these compounds. For

333 similar reason, the current parameterization does not include epoxy compounds or

334 anhydrides either.

335   In addition to the reference values, adjustment coefficients were introduced to

336 reflect the influence of different molecular structures more accurately on photolysis rate

337 constants. For example, when 2 methyl groups substitute both α-carbons of 3-pentanone

338 (forming 2,4-dimethyl-3-pentanone), the absorption significantly increases, likely due

339 to a redshift caused by the inductive effect of alkyl groups, resulting in an enhancement

340 of $0.36\% \, jNO_2$ for the photolysis frequencies (due to the lack of photolysis data for 3-

341 pentanone, 2-pentanone is used as a surrogate here). By identifying such relationships

删除了: is

343 and evaluating them against the corresponding reference values for their respective

344 carbon numbers, a total of ten adjustment coefficients have been introduced in the

345 current parameterization. The specific basis and calculation process for other

346 parameters can be found in Section S6 and Figure S31-S33 in the *Supplementary*

347 *Information*. The introduction of adjustment coefficients enhances the applicability and

348 accuracy of the parameterization for estimating photolysis rate constants of compounds

349 with diverse molecular structures.

350   Finally, to enable the estimation for a vast number of OVOCs, we developed a

351 program to automate structure recognition and photolysis frequency estimation, as

352 shown in Figure 4 for the workflow of the program. The program utilizes the SMILES

353 as the input format to identify the carbon count and characterize both the types and

354 quantities of functional groups. Then, the corresponding reference value and adjustment

355 coefficients from the pre-established dataset are retrieved to calculate and output the

356 predicted photolysis frequencies of the OVOC in the form of j_{rel}. This approach

357 effectively reproduces the j_{rel} of 104 compounds from the reference group of the

358 dataset (Figure 5a). The main deviations arise from underestimations for nitro-

359 naphthalene, 2-acetylbenzaldehyde, and 2-hexenal, as well as overestimation for

360 hydroxy butanone, highlighting areas for future optimization. Compared to the

361 measured data in the dataset, 81% of the species fall within a ±50% deviation range,

362 and 98% within a factor of 2 (Figure 5a). The strong agreement between measured and

363 predicted values ($R^2 = 0.92$) indicates the reliable performance of this proposed

364 parameterization method (Figure 5a).

365   For the 50 species in the comparison group, the estimated results from this study

366 align well with j_{rel} of approximately half of the species (Figure S5). Taking

367 nitrocatechols as an example, their j_{rel} were estimated based on those of structurally

368 similar nitrophenols, as both share aromatic rings substituted with OH and NO_2 groups.

369 The parameterization effectively reproduces the j_{rel} of four types of nitrocatechols

370 measured by Roman et al. (2022) using chamber experiments, further demonstrating

371 the reliable performance of the method. Notable deviations mainly originate from two

studies. Wang et al. (2023) reported significantly lower j_{rel} for three classes of monoterpene-derived organic nitrates, while Liu et al. (2018) estimated the j_{rel} of α-hydroperoxycarbonyls to be only about 7% of our estimated value. These differences can be explained by the substantial uncertainties in the comparison dataset, which was derived from eight independent studies that employed a variety of methodologies, such as quantum chemical calculations, single-wavelength measurements, and indirect estimates based on absorption cross-sections combined with assumed quantum yields. In addition, the current method does not incorporate structure-specific adjustments for certain compound classes, which may also contribute to the observed discrepancies.

3.2 Comparison to Master Chemical Mechanism v3.3.1

As a detailed mechanism, MCM includes 5809 species and intermediates, among which 2327 are classified as photodegradable. Our estimates of j_{rel} align with MCM within ±50% for 61% of the evaluated species (Figure 5b). Among all the photodegradable species in the MCM, two species (CH3SOOOH and ETOMENO3) are identified as non-photodegradable, as the method used is not applicable to sulfur-containing species and ETOMENO3 lack photoreactive chromophores. Consequently, no photolysis rate constants were generated for them. The differences in photolysis rate constants primarily arise from differences in the classification and estimation of functional groups for multifunctional compounds (Figure 5b). The parameterization method produces higher values for species such as aromatic aldehydes, multi-carbonyl compounds, nitrate esters, and hydroxyl nitrate esters, while it yields lower values for species including carbonyl hydroperoxides, unsaturated diketones, hydroxy nitrates, and hydroxycarboxylic acids when compared to MCM. The detailed estimation results for 2327 photodegradable species can be found in the "*Prediction-MCM2327*" sheet in the supplementary file. An updated MCM v3.3.1 mechanism that can be directly used in the F0AM box model is available in the file named "*MCMv331_OVOCshv_updated_Mech*" on the FigShare website (Peng, 2025).

In addition to these 2327 photodegradable species identified in MCM, this study further identifies 714 additional photodegradable species from the 5809 species in

MCM based on their structural characteristics. The 714 newly identified species are primarily characterized by their diverse chromophore, including carbonyl groups, nitrates (e.g., ONO_2, $C(=O)ONO_2$, $C(=O)OONO_2$), and hydroxyl groups (OH). A notable proportion (38%) of these species contain ring structures, suggesting their origin from aromatic hydrocarbon, terpenes, or other polycyclic compounds. Additionally, 46% of the newly identified species contain two or more chromophores, further emphasizing the need for more comprehensive evaluation of multifunctional species. The photolysis rate constants of these photolysis reactions were determined using the structure-based parameterization, while the reaction products were inferred based on existing patterns of known products, producing 1 to 2 radicals. Details of the newly coupled photolysis module with MCM v3.3.1 are provided in the "*714 Newly Add Species*" and "*Additional OVOCs Mech*" sheet in the supplementary file. A supplementary mechanism that can be directly used in the F0AM box model is available in the file named "*MCMv331_OVOCshv_updated_Mech* " on the FigShare website (Peng, 2025). Details on surrogate products for unknown photolysis reactions can be found in Section S7 of *Supplementary Information*. The modifications to photolysis reactions, including photolysis rate constants and reaction products are incorporated into the standard MCM v3.3.1 as a newly updated chemical mechanism

The application of the new photolysis mechanism has influenced both the concentration of photodegradable OVOCs and the relative contributions of their removal pathways. Compared to the standard MCM mechanism, a 50% or greater increase in the concentration of OVOCs was observed for 9% of photodegradable species at Guangzhou urban site, and for 16% at PRD regional site (Figure 6 (a, b)). Some species exhibited an increase in concentration even when photolysis was enhanced, which was observed for 9.2% of species at Guangzhou urban site, and for 11% at PRD regional site. This observation may be attributed to the positive feedback between the radicals generated by the enhanced photolysis of these OVOCs and the oxidation of their precursors, leading to the formation of additional photodegradable products. This effect is consistent with the findings of Qu et al. (2021), where OVOC

430 photolysis contribute to the amplification of radical cycling in the atmosphere.

431   The changes in concentrations of OVOCs reflect variations of their atmospheric

432 budget. Here, the ratio of $j_{OVOC}/(k_{OH} \times [OH])$ is used to represent the relative

433 importance of two pathways for each OVOC species: photolysis and reactions with OH

434 radicals (Figure 6 (c, d)). The ratio is calculated by dividing the photolysis removal rate

435 by the OH reaction removal rate for each species, and the campaign average is then

436 computed to obtain the mean ratio for each species. After adopting the new photolysis

437 scheme, the relative importance of photolysis increased for over half of the

438 photodegradable OVOCs species at both sites. For the campaign-averaged

439 $j_{OVOC}/(k_{OH} \times [OH])$, the new mechanism shows a 25% increase (from 1.2 to 1.5) at

440 Guangzhou urban site and a 21% increase (from 1.7 to 2.1) at PRD regional site. From

441 the perspective of the number of carbonyl functional group in each species, species

442 containing zero to one carbonyl group is removed from the atmosphere mainly via

443 reaction with OH radical rather than photolysis. For species containing two or more

444 carbonyls, photolysis dominates their atmospheric removal. The averaged

445 $j_{OVOC}/(k_{OH} \times [OH])$ for compounds with 2 or more carbonyls is 4.4 at the Guangzhou

446 urban site and 6.1 at the PRD regional site, indicating that photolysis is a more

447 important removal pathway than reaction with OH radicals for multi-carbonyl

448 compounds. At the Guangzhou urban site, the new mechanism increased the

449 $j_{OVOC}/(k_{OH} \times [OH])$ value by 34% for species with 0-1 carbonyls and by 188% for

450 species with more than three carbonyls, while the ratio decreased by 27% for species

451 with two carbonyls. Similar changes were observed at the PRD regional site. This

452 suggests that previous mechanisms may overestimate the photolysis of dicarbonyl

453 compounds, while underestimation for photolysis of multi-carbonyl compounds. Late-

454 generation VOC oxidation products, especially those with multiple carbonyl groups,

455 warrant further investigation into their role in photolysis as part of their atmospheric

456 removal pathway.

457   The updated mechanism not only influences OVOCs themselves but also affects

458 the production of ROx radicals in our simulations. A significant contribution from non-

HCHO OVOC photolysis to ROx radical production was observed at both sites, with an enhancement in p(ROx) upon application of the updated photolysis mechanism. After implementing the updated mechanism, the averaged daytime contribution of non-HCHO OVOCs photolysis to p(ROx) increased from 36% to 40% at the Guangzhou urban site (Figure 7). In contrast, the contribution from HCHO photolysis remained relatively low at 13%. Similarly, at the PRD regional site, the averaged daytime contribution of non-HCHO OVOCs photolysis increased from 44% to 47%, which is 2.6 times that of HCHO photolysis (Figure 7). As a result, the total daytime p(ROx) reached 2.9 ppb h^{-1} at the Guangzhou urban site and 3.7 ppb at the PRD regional site. Notably, at noon when ROx production peaked, p(ROx) showed an increase of 7.6% at the Guangzhou urban site and 8.8% at the PRD regional site. These findings highlight the dominant role of non-HCHO OVOCs photolysis in driving ROx radical production, surpassing the contribution from formaldehyde photolysis.

Under the influence of the new photolysis mechanism, more than 2000 OVOC species collectively contributed to changes in p(ROx) levels. The implementation of this new mechanism led to an increased contribution to p(ROx) from non-carbonyl-containing OVOCs (e.g., nitrophenols), unsaturated mono-carbonyl species (e.g., methacrolein, MACR), and saturated tri-carbonyl compounds (e.g., 3,4-dioxopentanal) at both sites (Figure 7 Comparison of the modeled contributions of different OVOC types to total p(ROx) at urban and regional sites under Scenario 1. Blue bars represent the urban site, while yellow bars represent the regional site. Error bars (this study only) show the range from using the maximum and minimum estimated photolysis rate constants in the simulations.

). The greatest absolute increase in p(ROx) was observed for unsaturated mono-carbonyl compounds at the PRD regional site, followed by non-carbonyl-containing OVOCs, with mean increases of 2.4 ppb d^{-1} and 1.0 ppb d^{-1}, respectively. In contrast, the contribution of unsaturated di-carbonyl compounds (e.g., 2-methylbutenedial) to p(ROx) decreased at both sites. The impact of the new photolysis mechanism was more pronounced at the PRD regional site, likely due to the higher fractions of OVOCs in downwind areas (Liang et al., 2022).

As radical production is increased using the new photolysis mechanism, ozone production is also enhanced. The enhancement of ozone production rate p(O$_3$) at noon was relatively modest, with increases of 5.3% at the urban site and 3.9% at the regional

493 site. Similarly, peroxyacetyl nitrate (PAN), a typical photochemical product, exhibited

494 minor sensitivity to the new mechanism, with noon concentrations increasing by 2.2%–

495 6.9% at both sites. This may result from modifications to the photolysis rate constants

496 of a wide range of OVOCs in the new mechanism, where the opposing effects of

497 increased and decreased rates effectively counterbalanced each other, masking the

498 impact of OVOCs photolysis on secondary species formation.

499 **3.3 Identifying key non-HCHO species contributing to p(ROx)**

500 Only HCHO concentrations were constrained in Scenario 1 of model simulation,

501 which may bear substantial biases within simulated concentrations of other

502 photodegradable OVOCs and hence influence identification of key species that

503 significantly contribute to p(ROx). For example, the new mechanism incorporated the

504 photolysis of nitrophenol, partially alleviating its overestimation, yet the simulated

505 concentrations remained significantly higher than observations (see Figure S7). This

506 residual overestimation may be attributed to enhanced secondary formation driven by

507 accelerated ROx cycling, as well as the absence of heterogeneous loss processes such

508 as particle-phase reactions and deposition. To identify key species among numerous

509 photodegradable OVOCs, Scenario 2 imposes extensive constraints on intermediate

510 products to approximate a "quasi-realistic" VOC composition. Under these conditions,

511 the impacts of the new photolysis mechanism on p(ROx) are investigated across three

512 different environments. OVOCs contributed over 50% of VOCs at all sites, with the

513 highest OVOC contribution at the PRD regional site (56%).

514 After constraining intermediate species in the model, non-HCHO OVOCs still

515 show a significant contribution to p(ROx). At the urban sites, non-HCHO OVOCs

516 contributed 27% (Guangzhou) and 25% (Beijing) to p(ROx), while at the PRD regional

517 site, this contribution was higher at 45%, with an average p(ROx) of 16 ppb d^{-1} (Figure

518 9 (a,c,e)). Despite similar j_{NO_2} values at the PRD regional site and the Guangzhou urban

519 site (Figure S8), the PRD regional site showed a significantly higher p(ROx), indicating

520 that higher OVOC concentrations and more aged air masses are key drivers of radical

521 production in the regional environment. This contrast suggests that under these

522 conditions, the composition and concentration of OVOCs play a more crucial role in

523 radical production than photolysis intensity.

524 Further analysis of the relative fractions reveals regional differences in the

525 contribution of non-HCHO OVOC photolysis to p(ROx) throughout the day. At the

526 PRD regional site, the contribution of non-HCHO OVOC increased with solar radiation,

527 peaking at 46% at noon, then stabilizing before declining after sunset (Figure 9 (d)).

528 This peak corresponds to maximum radiation, and the afternoon stability suggests

529 replenishment by the oxidation of transported VOCs from upwind megacities. In

530 contrast, the contribution at both urban sites peaked at 35% at 7 a.m. and then gradually

531 declined to 25%–30% before sharply dropping prior to sunset (Figure 9 (b, f)). The

532 morning peak is likely due to primary emissions or photolysis of overnight-

533 accumulated OVOCs, while lower daytime values reflect limited photodegradable

534 OVOCs in fresher air. In summary, the contribution of non-HCHO OVOC photolysis

535 to p(ROx) exhibited a unimodal diurnal pattern at the PRD regional site, while a

536 morning peak was observed at both urban sites.

537 An analysis of the contribution of non-HCHO OVOC photolysis to p(ROx) was

538 conducted based on the structure of OVOCs (Figure 10 (a, c, e)). Both urban sites

539 exhibited similar trends, with OVOCs containing a single carbonyl group dominating

540 their contribution to p(ROx). At the Beijing urban site, these mono-carbonyl OVOCs

541 accounted for nearly half of the non-HCHO OVOCs, most of which were saturated

542 compounds. Mono-carbonyls contributed approximately 13% to the total p(ROx) at the

543 Guangzhou urban site and 14% at the Beijing urban site, given that non-HCHO OVOCs

544 contributed around 27% and 25%, respectively. Di-carbonyl OVOCs contributed

545 second-most at both urban sites, mostly from saturated compounds, while compounds

546 with 3 to 5 carbonyl groups contributed 9%–12%. In contrast, di-carbonyl compounds

547 were the primary contributor at the PRD regional site, with an increased contribution

548 of unsaturated mono-carbonyls. Compounds with 3 to 5 carbonyl groups contributed

549 17% at the PRD regional site, significantly higher than at urban sites, highlighting the

550 role of more oxidized and multifunctional species in regional environments.

551 Compounds without carbonyl groups, such as nitrophenol and organic nitrates,

552 contributed minimally (5-8%) across all sites, likely due to lower concentrations or

553 slower photolysis rates. Generally, mono-carbonyl OVOCs dominate p(ROx) at urban

554 sites, while multiple carbonyl OVOCs are more important at the regional site.

555 From an individual species perspective, the top ten non-HCHO OVOCs

556 accounted for more than half of the total non-HCHO OVOC contribution to p(ROx) at

557 all sites (Figure 10 (b, d, f)). At urban sites, the contributions are primarily driven by

558 OVOCs containing 1-2 carbonyl groups, contributing 50% at the Guangzhou urban site

559 and 45% at the Beijing urban site. At the PRD regional site, contributions from di-

560 carbonyl and multi-carbonyl (3-4 carbonyl groups) compounds increased significantly.

561 The top ten non-HCHO OVOCs across all sites mainly included oxidation products

562 from alkenes, ring-retaining products and multi-carbonyl ring-opening products from

563 aromatic oxidation, as well as aldehydes. Notably, biogenic VOC oxidation products

564 such as those from isoprene and β-pinene (e.g., NOPINONE) were prominent at both

565 urban sites, highlighting the potential importance of BVOCs in OVOC formation in

566 urban areas. Although the individual contributions of the remaining OVOCs (over 2000

567 species) outside the top ten were small, their cumulative impact remained notable.

568 **4 Conclusion**

569 In this study, a structure-based parameterization for OVOCs photolysis rate

570 constants has been developed, together with an OVOCs photolysis mechanism

571 supplementary module based on the MCM v3.3.1 mechanism. The proposed method

572 effectively reproduces photolysis rate constants for 104 compounds using 21 reference

573 values and 10 adjustment coefficients. Additionally, it identifies 714 photodegradable

574 species not considered photolyzable in MCM v3.3.1. The integration of the new

575 photolysis mechanism leads to a 13% increase in p(ROx) at both Guangzhou urban site

576 and PRD regional sites, contributing 27% and 56% to daily p(ROx), respectively. For

577 multi-carbonyl compounds, photolysis contributes more to their atmospheric removal

578 than reactions with OH radicals. After innovatively using the model results to allocate

579 mass spectrometry data and constrain more intermediate species, the model still reveals

significant contributions of non-HCHO OVOC photolysis to p(ROx). Non-HCHO OVOC photolysis contributes 25%–27% to p(ROx) at both urban sites, and 45% at the PRD regional site, surpassing the contribution of HCHO photolysis. The diurnal variations in the fraction of p(ROx) contributed by non-HCHO OVOC photolysis highlight the importance of primary OVOC emissions at urban sites and the oxidation of transported VOCs at the PRD regional site. The top 10 species contribute over half of the non-HCHO OVOC contribution to p(ROx), while the remaining more than 2000 species collectively make a noteworthy contribution. Photolysis of multifunctional compounds produced from the oxidation of alkenes and aromatics plays a major role in radical production.

By establishing a relationship between species structure and photolysis frequencies, this study circumvents the limitation of insufficient quantum yield data, enabling the derivation of photolysis mechanisms for compounds whose photolysis frequencies have not been previously measured. The estimated rate constants, combined with species concentrations from model simulations, allow for the identification of key species that significantly contribute to radical production in different environments. This approach not only provides a species-specific evaluation of OVOCs photolysis, but also offers valuable insights for future laboratory experiments, field observations, and the optimization of chemical mechanisms. Nevertheless, some species remain insufficiently characterized in terms of their photolysis rate constants or mechanisms. For example, the photolysis rate constant of nitrophenol varies notably among different studies. The photolysis behavior of pinene oxidation products has been scarcely examined (Wang et al., 2023), and in this study, their mechanisms were surrogated by using those of cyclo-ketones. Additionally, several compounds with strong photolysis potential, such as alkyl nitrites and N-nitrosamines, are not yet included in the MCM mechanism and require further investigation. Research on multifunctional OVOCs, particularly multi-carbonyl compounds, is still limited. Future experimental efforts are expected to generate more comprehensive data, thereby refining the existing OVOCs photolysis mechanisms, and

609   ultimately enhancing our understanding of atmospheric chemistry.

610

Data and code availability

The observational data and parameterization tool-kit used in this study are available from corresponding authors upon request (byuan@jnu.edu.cn).

Author contributions

YWP, BY and MS designed the research. SHW, XS, WJW, SXY, JPQ, XJH, YBHF, XBL contributed to field campaign and data collection. YWP performed the data analysis and parameterization of photolysis data. YWP, BY, and MS prepared the manuscript. All the authors reviewed the manuscript.

Competing interests

The authors declare that they have no known competing financial interests or personal relationships that could have appeared to influence the work reported in this paper.

Acknowledgements

This work was supported by the National Natural Science Foundation of China (grant No. 42275103, 42121004) and National Key Research and Development Program of China (grant No. 2023YFC3706200).

Appendix A. Supplementary Information

Supporting information to this article can be found at …

References

Aumont, B., Szopa, S., and Madronich, S.: Modelling the evolution of organic carbon during its gas-phase tropospheric oxidation: development of an explicit model based on a self generating approach, Atmospheric Chemistry and Physics, 5, 2497-2517, 10.5194/acp-5-2497-2005, 2005.

Bloss, C., Wagner, V., Jenkin, M., Volkamer, R., Bloss, W., Lee, J., Heard, D., Wirtz, K., Martin-Reviejo, M., and Rea, G.: Development of a detailed chemical mechanism (MCMv3.1) for the atmospheric oxidation of aromatic hydrocarbons, Atmospheric Chemistry and Physics, 5, 641-664, https://doi.org/10.5194/acp-5-641-2005, 2005.

Cai, M., Ye, C., Yuan, B., Huang, S., Zheng, E., Yang, S., Wang, Z., Lin, Y., Li, T., Hu, W., Chen, W., Song, Q., Li, W., Peng, Y., Liang, B., Sun, Q., Zhao, J., Chen, D., Sun, J., Yang, Z., and Shao, M.: Enhanced daytime secondary aerosol formation driven by gas–particle partitioning in downwind urban plumes, Atmospheric Chemistry and Physics, 24, 13065-13079, 2024.

Calvert, J. G., Mellouki, A., Orlando, J. J., Pilling, M. J., and Wallington, T. J.: Mechanisms of Photodecomposition of the Sunlight-Absorbing Oxygenates, in: Mechanisms of Atmospheric Oxidation of the Oxygenates, Oxford University Press, 974-1357, 2011.

Calvert, J. G., Atkinson, R., Becker, K. H., Kamens, R. M., Seinfeld, J. H., Wallington, T. H., and Yarwood, G.: Primary photochemical processes of the aromatic hydrocarbons and some of their common oxidation products, in: The Mechanisms of Atmospheric Oxidation of the Aromatic Hydrocarbons, Oxford University Press, 230-310, 2002.

Carter, W. P. L., Jiang, J., Orlando, J. J., and Barsanti, K. C.: Derivation of atmospheric reaction mechanisms for volatile organic compounds by the SAPRC mechanism generation system (MechGen), Atmospheric Chemistry and Physics, 25, 199-242, 10.5194/acp-25-199-2025, 2025.

Chen, Y., Zheng, P., Wang, Z., Pu, W., Tan, Y., Yu, C., Xia, M., Wang, W., Guo, J., Huang, D., Yan, C., Nie, W., Ling, Z., Chen, Q., Lee, S., and Wang, T.: Secondary Formation and Impacts of Gaseous Nitro-Phenolic Compounds in the Continental Outflow Observed at a Background Site in South China, Environmental Science & Technology, 56, 6933-6943, 10.1021/acs.est.1c04596, 2022.

Edwards, P. M., Brown, S. S., Roberts, J. M., Ahmadov, R., Banta, R. M., deGouw, J. A., Dube, W. P., Field, R. A., Flynn, J. H., Gilman, J. B., Graus, M., Helmig, D., Koss, A., Langford, A. O., Lefer, B. L., Lerner, B. M., Li, R., Li, S. M., McKeen, S. A., Murphy, S. M., Parrish, D. D., Senff, C. J., Soltis, J., Stutz, J., Sweeney, C., Thompson, C. R., Trainer, M. K., Tsai, C., Veres, P. R., Washenfelder, R. A., Warneke, C., Wild, R. J., Young, C. J., Yuan, B., and Zamora, R.: High winter ozone pollution from carbonyl photolysis in an oil and gas basin, Nature, 514, 351-354, 10.1038/nature13767, 2014.

Eger, P. G., Schuladen, J., Sobanski, N., Fischer, H., Karu, E., Williams, J., Riva, M.,

Zha, Q., Ehn, M., and Quéléver, L. L.: Pyruvic acid in the boreal forest: gas-phase mixing ratios and impact on radical chemistry, Atmospheric Chemistry and Physics, 20, 3697-3711, 2020.

Griffith, S. M., Hansen, R., Dusanter, S., Michoud, V., Gilman, J., Kuster, W., Veres, P., Graus, M., de Gouw, J., and Roberts, J.: Measurements of hydroxyl and hydroperoxy radicals during CalNex-LA: Model comparisons and radical budgets, Journal of Geophysical Research: Atmospheres, 121, 4211-4232, 2016.

He, X., Yuan, B., Wu, C., Wang, S., Wang, C., Huangfu, Y., Qi, J., Ma, N., Xu, W., Wang, M., Chen, W., Su, H., Cheng, Y., and Shao, M.: Volatile organic compounds in wintertime North China Plain: Insights from measurements of proton transfer reaction time-of-flight mass spectrometer (PTR-ToF-MS), Journal of Environmental Sciences, 114, 98-114, 10.1016/j.jes.2021.08.010, 2022.

Huang, X.-F., Zhang, B., Xia, S.-Y., Han, Y., Wang, C., Yu, G.-H., and Feng, N.: Sources of oxygenated volatile organic compounds (OVOCs) in urban atmospheres in North and South China, Environmental Pollution, 261, 114152, 2020.

Huangfu, Y., Yuan, B., He, X., Liu, Z., Zhang, Y., Karl, T., Striednig, M., Ding, Y., Chen, X., and Li, H.: Natural Gas Leakage Ratio Determined from Flux Measurements of Methane in Urban Beijing, Environmental Science & Technology Letters, 11, 1025-1031, 2024.

Hui, L., Liu, X., Tan, Q., Feng, M., An, J., Qu, Y., Zhang, Y., and Jiang, M.: Characteristics, source apportionment and contribution of VOCs to ozone formation in Wuhan, Central China, Atmospheric Environment, 192, 55-71, 10.1016/j.atmosenv.2018.08.042, 2018.

IUPAC: IUPAC Task Group on Atmospheric Chemical Kinetic Data Evaluation, International Union of Pure and Applied Chemistry [dataset], 2012.

Jenkin, M., Saunders, S., Wagner, V., and Pilling, M.: Protocol for the development of the Master Chemical Mechanism, MCM v3 (Part B): tropospheric degradation of aromatic volatile organic compounds, Atmospheric Chemistry and Physics, 3, 181-193, 2003.

Jenkin, M. E., Saunders, S. M., and Pilling, M. J.: The tropospheric degradation of volatile organic compounds: a protocol for mechanism development, 1997.

Jenkin, M. E., Young, J. C., and Rickard, A. R.: The MCM v3.3.1 degradation scheme for isoprene, Atmospheric Chemistry and Physics, 15, 11433-11459, 10.5194/acp-15-11433-2015, 2015.

Jing, S.-A., Gao, Y.-Q., Shen, J.-D., Wang, Q., Peng, Y.-R., Li, Y.-J., and Wang, H.-L.: Characteristics and reactivity of ambient VOCs in urban Hangzhou, China, Environmental Science, 41, 5306-5315, 2020.

Kanaya, Y., Cao, R., Akimoto, H., Fukuda, M., Komazaki, Y., Yokouchi, Y., Koike, M., Tanimoto, H., Takegawa, N., and Kondo, Y.: Urban photochemistry in central Tokyo: 1. Observed and modeled OH and HO_2 radical concentrations during the winter and summer of 2004, Journal of Geophysical Research: Atmospheres, 112, 2007.

Keller-Rudek, H., Moortgat, G. K., Sander, R., and Sörensen, R.: The MPI-Mainz UV/VIS Spectral Atlas of Gaseous Molecules of Atmospheric Interest, Earth System Science Data, 5, 365-373, 10.5194/essd-5-365-2013, 2013.

Kroll, J. H., Donahue, N. M., Jimenez, J. L., Kessler, S. H., Canagaratna, M. R., Wilson, K. R., Altieri, K. E., Mazzoleni, L. R., Wozniak, A. S., Bluhm, H., Mysak, E. R., Smith, J. D., Kolb, C. E., and Worsnop, D. R.: Carbon oxidation state as a metric for describing the chemistry of atmospheric organic aerosol, Nature Chemistry, 3, 133-139, 10.1038/nchem.948, 2011.

Lantz, K. O., Shetter, R. E., Cantrell, C. A., Flocke, S. J., Calvert, J. G., and Madronich, S.: Theoretical, actinometric, and radiometric determinations of the photolysis rate coefficient of NO_2 during the Mauna Loa Observatory Photochemistry Experiment 2, Journal of Geophysical Research: Atmospheres, 101, 14613-14630, https://doi.org/10.1029/96JD00215, 1996.

Li, K., Jacob, D. J., Liao, H., Qiu, Y., Shen, L., Zhai, S., Bates, K. H., Sulprizio, M. P., Song, S., and Lu, X.: Ozone pollution in the North China Plain spreading into the late-winter haze season, Proceedings of the National Academy of Sciences, 118, e2015797118, 2021.

Li, X. B., Yuan, B., Huangfu, Y., Yang, S., Song, X., Qi, J., He, X., Wang, S., Chen, Y., Yang, Q., Song, Y., Peng, Y., Tang, G., Gao, J., Gu, D., and Shao, M.: Vertical changes in volatile organic compounds (VOCs) and impacts on photochemical ozone formation, Atmospheric Chemistry and Physics, 25, 2459-2472, 10.5194/acp-25-2459-2025, 2025.

Li, Y., Yin, S., Yu, S., Yuan, M., Dong, Z., Zhang, D., Yang, L., and Zhang, R.: Characteristics, source apportionment and health risks of ambient VOCs during high ozone period at an urban site in central plain, China, Chemosphere, 250, 126283, 2020.

Liang, Y., Weber, R. J., Misztal, P. K., Jen, C. N., and Goldstein, A. H.: Aging of volatile organic compounds in October 2017 northern California wildfire plumes, Environmental science & technology, 56, 1557-1567, 2022.

Liu, Y., Song, M., Liu, X., Zhang, Y., Hui, L., Kong, L., Zhang, Y., Zhang, C., Qu, Y., and An, J.: Characterization and sources of volatile organic compounds (VOCs) and their related changes during ozone pollution days in 2016 in Beijing, China, Environmental Pollution, 257, 113599, 2020.

Liu, Z., Nguyen, V. S., Harvey, J., Müller, J.-F., and Peeters, J.: The photolysis of α-hydroperoxycarbonyls, Physical Chemistry Chemical Physics, 20, 6970-6979, 10.1039/c7cp08421h, 2018.

Liu, Z., Wang, Y., Gu, D., Zhao, C., Huey, L. G., Stickel, R., Liao, J., Shao, M., Zhu, T., and Zeng, L.: Summertime photochemistry during CAREBeijing-2007: ROx budgets and O_3 formation, Atmospheric Chemistry and Physics, 12, 7737-7752, 2012.

Madronich, S. and Flocke, S.: The role of solar radiation in atmospheric chemistry, in: Environmental Photochemistry, 1 ed., edited by: Boule, P., Springer Berlin, Heidelberg, 1-26, https://10.1007/978-3-540-69044-3_1, 1999.

McDonald, B. C., De Gouw, J. A., Gilman, J. B., Jathar, S. H., Akherati, A., Cappa, C.

D., Jimenez, J. L., Lee-Taylor, J., Hayes, P. L., and McKeen, S. A.: Volatile chemical products emerging as largest petrochemical source of urban organic emissions, Science, 359, 760-764, 2018.

Mellouki, A., Wallington, T., and Chen, J.: Atmospheric chemistry of oxygenated volatile organic compounds: impacts on air quality and climate, Chemical Reviews, 115, 3984-4014, 2015.

Mellouki, A., Ammann, M., Cox, R. A., Crowley, J. N., Herrmann, H., Jenkin, M. E., McNeill, V. F., Troe, J., and Wallington, T. J.: Evaluated kinetic and photochemical data for atmospheric chemistry: volume VIII–gas-phase reactions of organic species with four, or more, carbon atoms ($\geq C_4$), Atmospheric Chemistry and Physics, 21, 4797-4808, 2021.

Müller, J. F., Peeters, J., and Stavrakou, T.: Fast photolysis of carbonyl nitrates from isoprene, Atmospheric Chemistry and Physics, 14, 2497-2508, 10.5194/acp-14-2497-2014, 2014.

Newland, M. J., Rea, G. J., Thuner, L. P., Henderson, A. P., Golding, B. T., Rickard, A. R., Barnes, I., and Wenger, J.: Photochemistry of 2-butenedial and 4-oxo-2-pentenal under atmospheric boundary layer conditions, Physical Chemistry Chemical Physics, 21, 1160-1171, 10.1039/c8cp06437g, 2019.

Peng, Y.: MCMv331_OVOCshv_updated_Mech, figshare [code], 10.6084/m9.figshare.28743071.v1, 2025.

Peng, Y. W., Yuan, B., Yang, S. X., Wang, S. H., Yang, X. Y., Wang, W. J., Li, J., Song, X., Wu, C. H., Qi, J. P., Zheng, E., Ye, C. S., Huang, S., Hu, W. W., Song, W., Wang, X. M., Wang, B. L., and Shao, M.: Photolysis frequency of nitrophenols derived from ambient measurements, Science of the Total Environment, 869, 161810, 10.1016/j.scitotenv.2023.161810, 2023.

Qu, H., Wang, Y., Zhang, R., Liu, X., Huey, L. G., Sjostedt, S., Zeng, L., Lu, K., Wu, Y., and Shao, M.: Chemical production of oxygenated volatile organic compounds strongly enhances boundary-layer oxidation chemistry and ozone production, Environmental Science & Technology, 55, 13718-13727, 2021.

Riedel, T. P., Wolfe, G. M., Danas, K. T., Gilman, J. B., Kuster, W. C., Bon, D. M., Vlasenko, A., Li, S. M., Williams, E. J., Lerner, B. M., Veres, P. R., Roberts, J. M., Holloway, J. S., Lefer, B., Brown, S. S., and Thornton, J. A.: An MCM modeling study of nitryl chloride ($ClNO_2$) impacts on oxidation, ozone production and nitrogen oxide partitioning in polluted continental outflow, Atmospheric Chemistry and Physics, 14, 3789-3800, 10.5194/acp-14-3789-2014, 2014.

Roman, C., Arsene, C., Bejan, I. G., and Olariu, R. I.: Investigations into the gas-phase photolysis and OH radical kinetics of nitrocatechols: implications of intramolecular interactions on their atmospheric behaviour, Atmospheric Chemistry and Physics, 22, 2203-2219, 10.5194/acp-22-2203-2022, 2022.

Song, X., Bin, Y., Si-hang, W., Xian-jun, H., Xiao-bing, L., Yu-wen, P., Yu-bin, C., Ji-peng, Q., Jia-hua, C., Shan, H., dan, H., Wen, W., Ke-xuan, L., and Min, S.: Compositional Characteristics of Volatile Organic Compounds in Typical Industrial Areas of the Pearl River Delta: Importance of Oxygenated Volatile

805   Organic Compounds, Environmental Science, 44, 1336-1345,
806   10.13227/j.hjkx.202204104, 2023.

807 Tadić, J., Juranić, I., and Moortgat, G. K.: Pressure dependence of the photooxidation
808   of selected carbonyl compounds in air: n-butanal and n-pentanal, Journal of
809   Photochemistry And Photobiology A: Chemistry, 143, 169-179, 2001.

810 Tan, Z., Lu, K., Hofzumahaus, A., Fuchs, H., Bohn, B., Holland, F., Liu, Y., Rohrer, F.,
811   Shao, M., and Sun, K.: Experimental budgets of OH, HO_2, and RO_2 radicals
812   and implications for ozone formation in the Pearl River Delta in China 2014,
813   Atmospheric Chemistry and Physics, 19, 7129-7150, 2019a.

814 Tan, Z., Lu, K., Jiang, M., Su, R., Wang, H., Lou, S., Fu, Q., Zhai, C., Tan, Q., and Yue,
815   D.: Daytime atmospheric oxidation capacity in four Chinese megacities
816   during the photochemically polluted season: a case study based on box model
817   simulation, Atmospheric Chemistry and Physics, 19, 3493-3513, 2019b.

818 Tomas, A., Aslan, L., Muñoz, A., Ródenas, M., Vera, T., Borrás, E., Coddeville, P., and
819   Fittschen, C.: Photolysis of multifunctional carbonyl compounds under
820   natural irradiation at EUPHORE, Atmospheric Environment, 253, 118352,
821   10.1016/j.atmosenv.2021.118352, 2021.

822 Treves, K. and Rudich, Y.: The Atmospheric Fate of C_3-C_6 Hydroxyalkyl Nitrates, The
823   Journal of Physical Chemistry A, 107, 7809-7817, 2003.

824 Wang, C. M., Yuan, B., Wu, C. H., Wang, S. H., Qi, J. P., Wang, B. L., Wang, Z. L., Hu,
825   W. W., Chen, W., Ye, C. S., Wang, W. J., Sun, Y. L., Wang, C., Huang, S.,
826   Song, W., Wang, X. M., Yang, S. X., Zhang, S. Y., Xu, W. Y., Ma, N., Zhang,
827   Z. Y., Jiang, B., Su, H., Cheng, Y. F., Wang, X. M., and Shao, M.:
828   Measurements of higher alkanes using NO^+ chemical ionization in PTR-ToF-
829   MS: important contributions of higher alkanes to secondary organic aerosols
830   in China, Atmospheric Chemistry and Physics, 20, 14123-14138,
831   10.5194/acp-20-14123-2020, 2020.

832 Wang, S., Fan, B., and Dong, X.: Introduction to specification of SMILES and review
833   of its effect of chemical toxicity prediction, Occupational Health And
834   Emergency Rescue, 36, 471, 10.16369/j.oher.issn.1007-1326.2018.05.028,
835   2018.

836 Wang, W., Yuan, B., Peng, Y., Su, H., Cheng, Y., Yang, S., Wu, C., Qi, J., Bao, F.,
837   Huangfu, Y., Wang, C., Ye, C., Wang, Z., Wang, B., Wang, X., Song, W., Hu,
838   W., Cheng, P., Zhu, M., Zheng, J., and Shao, M.: Direct observations indicate
839   photodegradable oxygenated volatile organic compounds (OVOCs) as larger
840   contributors to radicals and ozone production in the atmosphere, Atmospheric
841   Chemistry and Physics, 22, 4117-4128, 10.5194/acp-22-4117-2022, 2022.

842 Wang, Y., Takeuchi, M., Wang, S., Nizkorodov, S. A., France, S., Eris, G., and Ng, N.
843   L.: Photolysis of gas-phase atmospherically relevant monoterpene-derived
844   organic nitrates, The Journal of Physical Chemistry A, 127, 987-999, 2023.

845 Weininger, D.: SMILES, a chemical language and information system. 1. Introduction
846   to methodology and encoding rules, Journal of Chemical Information and
847   Computer Sciences, 28, 31-36, 1988.

848 Wolfe, G. M., Marvin, M. R., Roberts, S. J., Travis, K. R., and Liao, J.: The Framework

849   for 0-D Atmospheric Modeling (F0AM) v3.1, Geoscientific Model
850   Development, 9, 3309-3319, 10.5194/gmd-9-3309-2016, 2016.
851 Wu, C., Wang, C., Wang, S., Wang, W., Yuan, B., Qi, J., Wang, B., Wang, H., Wang, C.,
852   Song, W., Wang, X., Hu, W., Lou, S., Ye, C., Peng, Y., Wang, Z., Huangfu, Y.,
853   Xie, Y., Zhu, M., Zheng, J., Wang, X., Jiang, B., Zhang, Z., and Shao, M.:
854   Measurement report: Important contributions of oxygenated compounds to
855   emissions and chemistry of volatile organic compounds in urban air,
856   Atmospheric Chemistry and Physics, 20, 14769-14785, 10.5194/acp-20-
857   14769-2020, 2020.
858 Yang, Q., Li, X. B., Yuan, B., Zhang, X., Huangfu, Y., Yang, L., He, X., Qi, J., and Shao,
859   M.: Measurement report: Enhanced photochemical formation of formic and
860   isocyanic acids in urban regions aloft – insights from tower-based online
861   gradient measurements, Atmospheric Chemistry and Physics, 24, 6865-6882,
862   10.5194/acp-24-6865-2024, 2024.
863 Yang, S., Yuan, B., Peng, Y., Huang, S., Chen, W., Hu, W., Pei, C., Zhou, J., Parrish, D.
864   D., Wang, W., He, X., Cheng, C., Li, X.-B., Yang, X., Song, Y., Wang, H., Qi,
865   J., Wang, B., Wang, C., Wang, C., Wang, Z., Li, T., Zheng, E., Wang, S., Wu,
866   C., Cai, M., Ye, C., Song, W., Cheng, P., Chen, D., Wang, X., Zhang, Z., Wang,
867   X., Zheng, J., and Shao, M.: The formation and mitigation of nitrate pollution:
868   comparison between urban and suburban environments, Atmospheric
869   Chemistry and Physics, 22, 4539-4556, 10.5194/acp-22-4539-2022, 2022.
870 Yang, X., Xue, L., Wang, T., Wang, X., Gao, J., Lee, S., Blake, D. R., Chai, F., and
871   Wang, W.: Observations and explicit modeling of summertime carbonyl
872   formation in Beijing: identification of key precursor species and their impact
873   on atmospheric oxidation chemistry, Journal of Geophysical Research:
874   Atmospheres, 123, 1426-1440, 2018.
875 Ye, C., Yuan, B., Lin, Y., Wang, Z., Hu, W., Li, T., Chen, W., Wu, C., Wang, C., Huang,
876   S., Qi, J., Wang, B., Wang, C., Song, W., Wang, X., Zheng, E., Krechmer, J.
877   E., Ye, P., Zhang, Z., Wang, X., Worsnop, D. R., and Shao, M.: Chemical
878   characterization of oxygenated organic compounds in the gas phase and
879   particle phase using iodide CIMS with FIGAERO in urban air, Atmospheric
880   Chemistry and Physics, 21, 8455-8478, 10.5194/acp-21-8455-2021, 2021.
881 Young, C. J., Washenfelder, R. A., Roberts, J. M., Mielke, L. H., Osthoff, H. D., Tsai,
882   C., Pikelnaya, O., Stutz, J., Veres, P. R., and Cochran, A. K.: Vertically
883   resolved measurements of nighttime radical reservoirs in Los Angeles and
884   their contribution to the urban radical budget, Environmental Science &
885   Technology, 46, 10965-10973, 2012.
886 Yuan, B., Koss, A. R., Warneke, C., Coggon, M., Sekimoto, K., and de Gouw, J. A.:
887   Proton-transfer-reaction mass spectrometry: applications in atmospheric
888   sciences, Chemical Reviews, 117, 13187-13229,
889   https://doi.org/10.1021/acs.chemrev.7b00325, 2017.
890 Yuan, B., Liggio, J., Wentzell, J., Li, S. M., Stark, H., Roberts, J. M., Gilman, J., Lerner,
891   B., Warneke, C., Li, R., Leithead, A., Osthoff, H. D., Wild, R., Brown, S. S.,
892   and de Gouw, J. A.: Secondary formation of nitrated phenols: insights from

observations during the Uintah Basin Winter Ozone Study (UBWOS) 2014, Atmospheric Chemistry and Physics, 16, 2139-2153, 10.5194/acp-16-2139-2016, 2016.

Figures

899
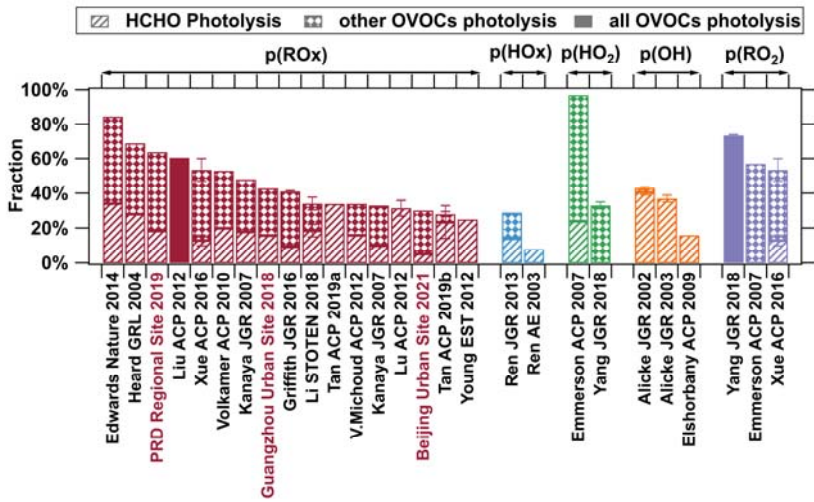
Figure 1 Contributions of OVOC photolysis to the production rates of radicals in different environments. ROx represents the sum of HO$_2$, RO$_2$, and OH, while HOx is the sum of HO$_2$ and OH. The contributions of OVOCs photolysis at the three sites determined in this study are shown in red. Detailed data, locations, season and year of the measurements, and references are provided in Table S1.

905

906
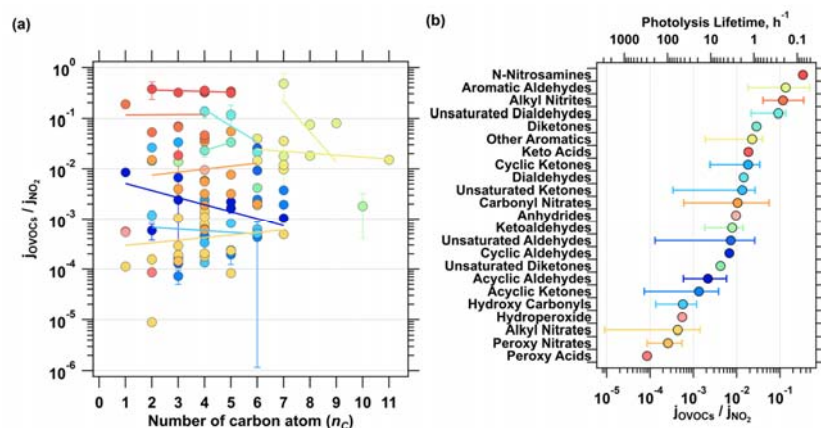
Figure 2 Relationship between the relative photolysis rate constants of OVOCs and the number of carbon atoms (a), and the range of relative photolysis rate constants for different categories of OVOCs after averaging with each class (b). The top axis of subplot (b) indicates the corresponding lifetimes against photolysis under overhead sun conditions, based on the j_{rel}, as a reference.
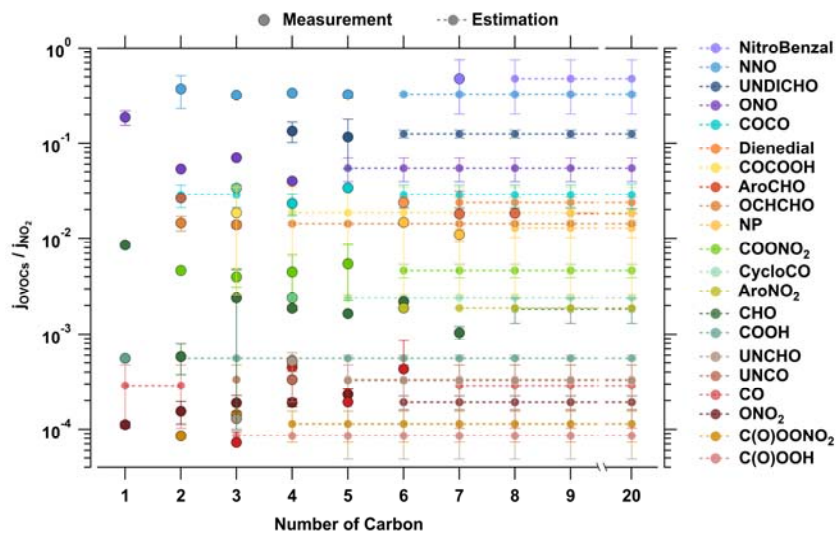
Figure 3 Variation of photolysis reference values of 21 different classes of OVOCs with the numbers of carbons in the molecules. The scatter points in the figure represent measured values from the dataset, while the dashed lines and the points connected by them indicate predicted values for the higher carbon-containing species.
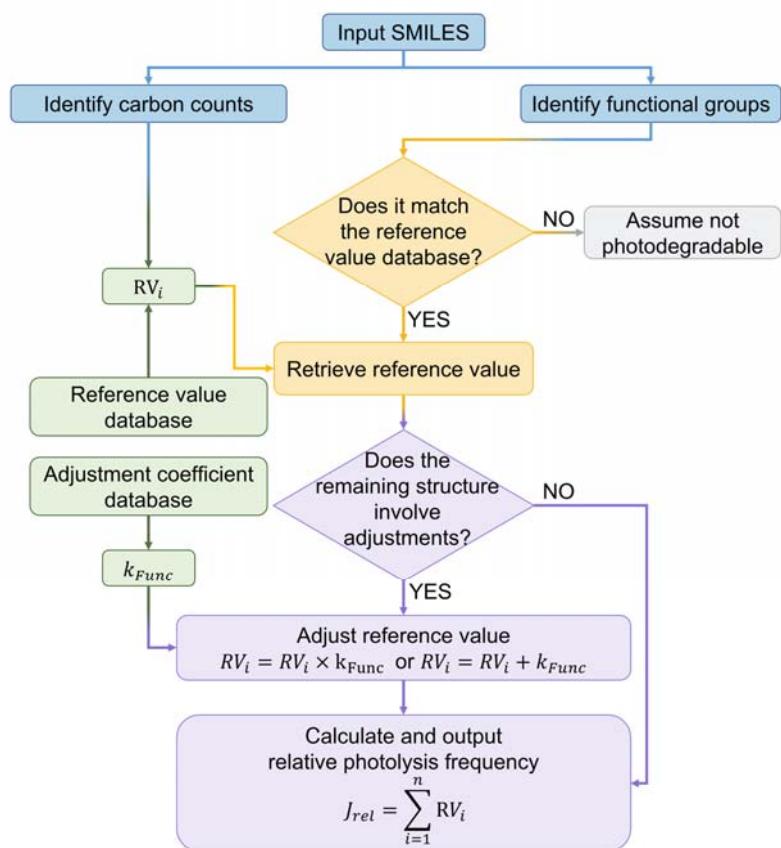
920
Figure 4 Flowchart of structural-based photolysis frequency parameterization.
922

923
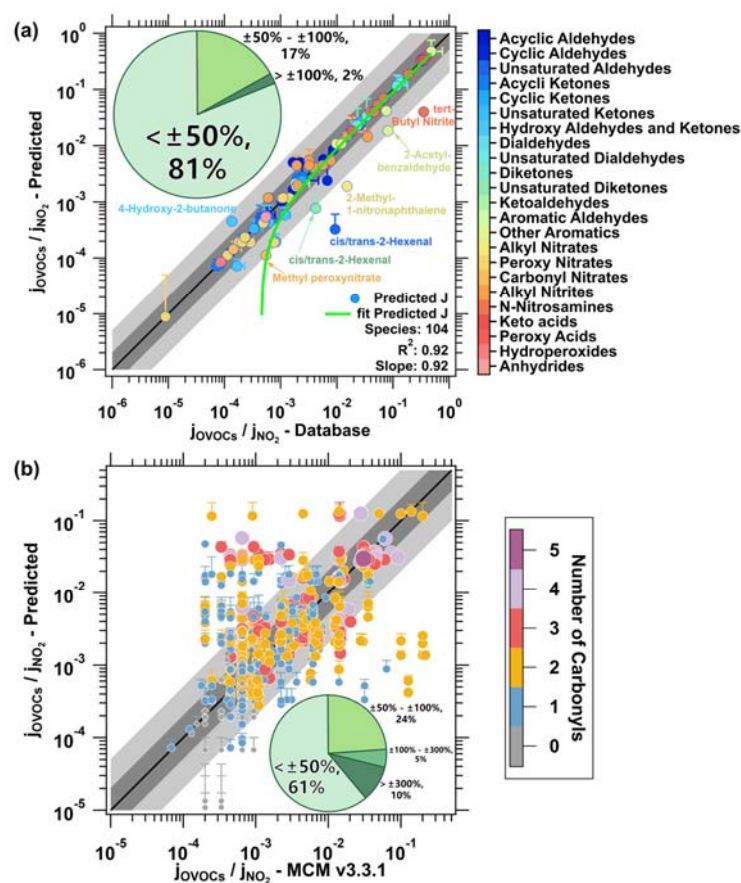
Figure 5 Comparison of predicted j_{rel} in this study and the measured j_{rel} in the reference group (a) or the j_{rel} in the MCM v3.3.1 mechanism. Each point corresponds to a specific compound, with species showing larger deviations labeled for clarity. The green curve in subplot (a) represents the fitted prediction. Different colors and sizes of the points in subplot (b) represent the number of carbonyl groups in each species. The black line indicates the 1:1 agreement and the darker gray band represents deviation of a factor of 2, while the lighter gray band extends to deviation for a factor of 5. The subplot pie chart illustrates the distribution of the relative deviation, calculated as $(predicted - measured)/measured$.

933

934
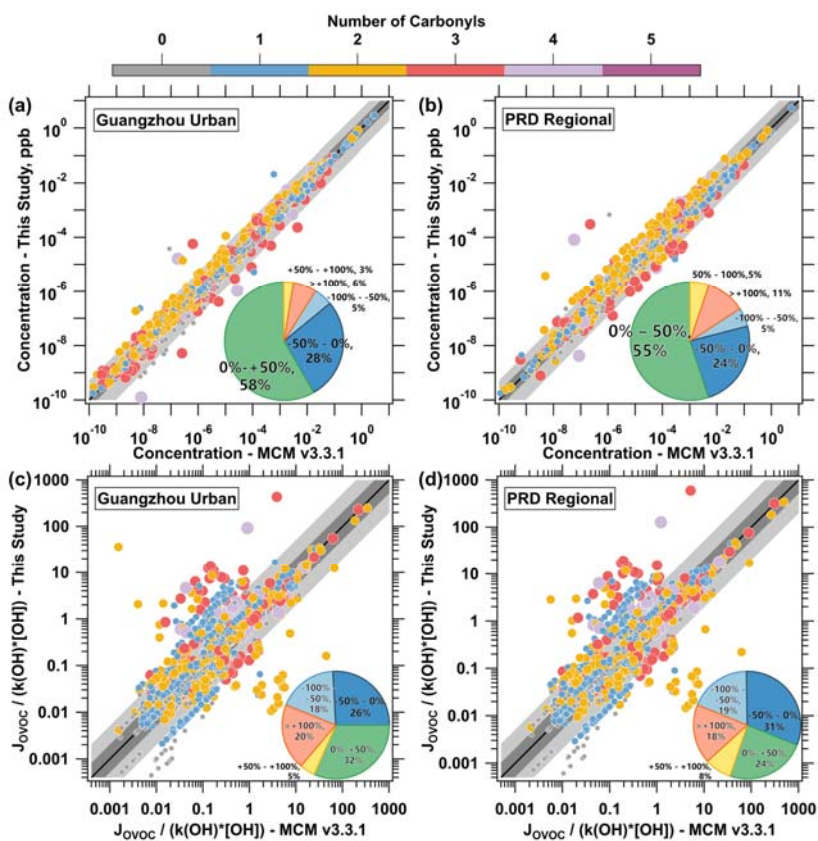
Figure 6 Comparison of concentration of photodegradable species (a, b), and the ratio of $j_{OVOC}/(k_{OH} \times [OH])$ (c, d) in the MCM V3.3.1 mechanism and predictions from this study in Scenario 1. Each point represents a specific compound. Different colors and sizes of the points represent the number of carbonyl groups in each species. The black line indicates the 1:1 agreement and the darker gray band represents deviation of a factor of 2, while the lighter gray band extends to deviation for a factor of 5. The subplot pie chart illustrates the distribution of the relative deviation, calculated as $(This\ Study - MCM)/MCM$.
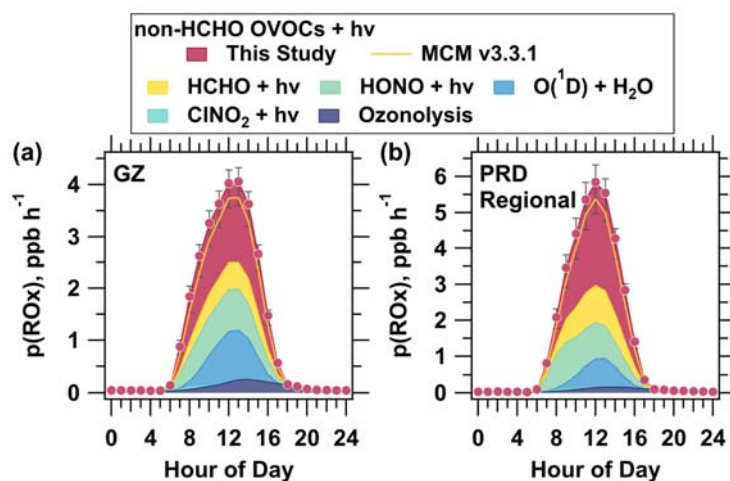
943

Figure 7 Comparison of the modeled contributions of different OVOC types to total p(ROx) at urban and regional sites under Scenario 1. Blue bars represent the urban site, while yellow bars represent the regional site. Error bars (this study only) show the range from using the maximum and minimum estimated photolysis rate constants in the simulations.

949

950
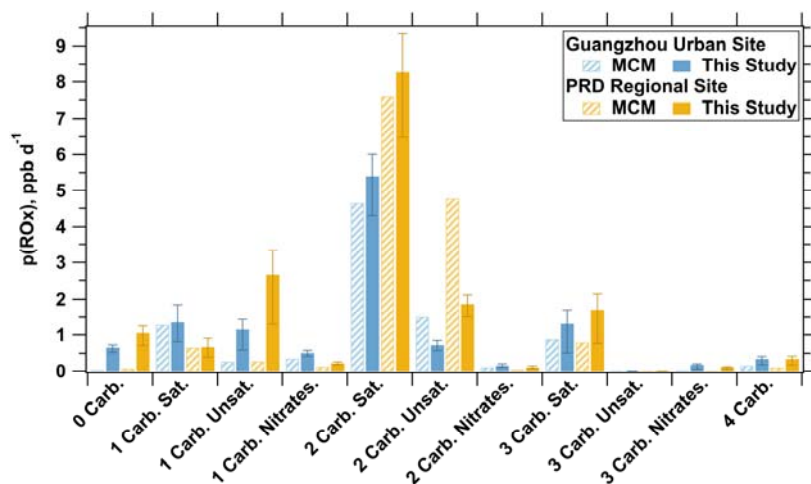
Figure 8 Comparison of the modeled contributions of different OVOC types to total p(ROx) at urban and regional sites under Scenario 1. Blue bars represent the urban site, while yellow bars represent the regional site. Error bars (this study only) show the range from using the maximum and minimum estimated photolysis rate constants in the simulations.

956

957
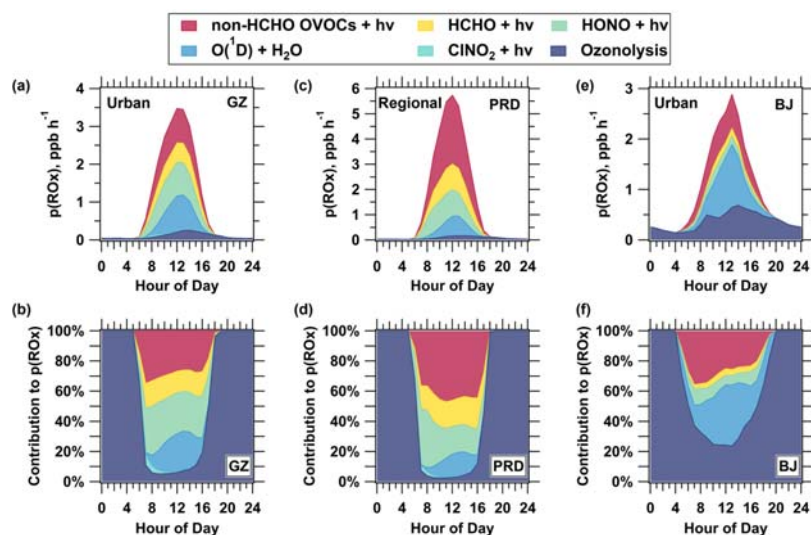
Figure 9 Source composition and pathway contributions of total p(ROx) at three sites under scenario 2. The first row (a, c, e) represents the p(ROx) source composition at the Guangzhou urban site (GZ, a), PRD regional site (PRD, c), and Beijing urban site (BJ, e), respectively. The second row (b, d, f) shows the contributions of different pathways to p(ROx) at the corresponding sites.

963

964
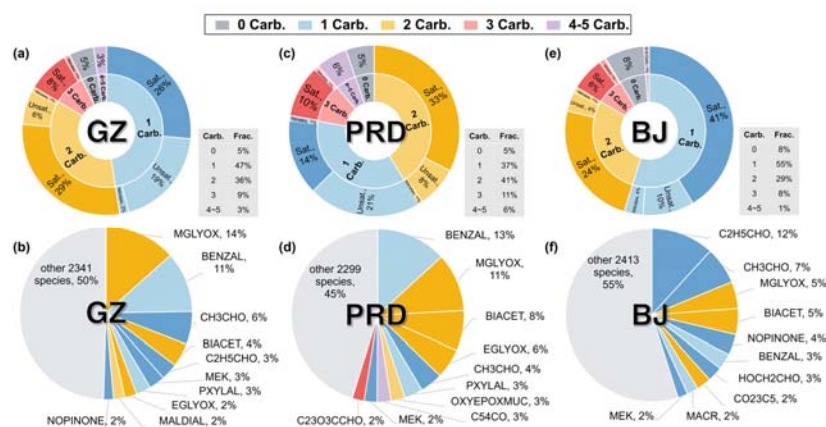
Figure 10 Contribution of OVOCs with different carbonyl counts to p(ROx) and the top 10 contributing species in Scenario 2. The first row (a, c, e) shows the fraction of OVOCs with different numbers of carbonyl groups, where **Sat.** stands for saturated, **Unsat.** for unsaturated, and **Nitrates** represents organic nitrates. Similar colors indicate species with the same number of carbonyl groups. The gray table at the bottom right of the sunburst chart displays the total fraction for each category of carbonyl groups. The second row (b, d, f) presents the MCM names and specific contributions of the top 10 contributing species. Results for the Guangzhou urban site are shown in (a, b), for the PRD regional site in (c, d), and for the Beijing urban site in (e, f).